Z. Physik A 273, 359–371 (1975)

Shock Waves and Mach Cones in Fast Nucleus-Nucleus Collisions*

H.G. Baumgardt, J.U. Schott, Y. Sakamoto**, and E. Schopper

Institut für Kernphysik, Johann Wolfgang Goethe-Universität, Frankfurt am Main, Germany

H. Stöcker, J. Hofmann, W. Scheid, and W. Greiner

Institut für Theoretische Physik, Johann Wolfgang Goethe-Universität, Frankfurt am Main, Germany

Received April 1, accepted April 4, 1975

Abstract. Mach shock waves and head shock waves occur during the interpenetration of a light high energetic nucleus with a heavy one. Collisions of ^{16}O, ^{12}C and ^{4}He ions at energies between 0.25 and 2.1 GeV/N with Ag and Cl nuclei have been investigated. The theoretical concepts and the experiment are presented and interpreted. From that a velocity of first sound in nuclear matter $c_s \approx 0.19c$, a Mach shock velocity $v_s \approx 0.58c$ and a nuclear compression constant $K = 300$ MeV are deduced.

1. Introduction

If nuclei collide with the relative velocity v larger than the velocity c_s of first sound in nuclear matter, shock waves are predicted to develop [1, 2]. They are of principal importance, because of the rather high densities ($\rho/\rho_0 \approx 2$–5) and temperatures ($T \approx 30$–200 MeV) expected in the shock zones and the thus developing isobaric and hot matter with properties which are completely unknown at present, and because of the possibility to investigate the energy density functional $W(\rho, T)$ of nuclear matter far beyond the equilibrium point $\rho = \rho_0$. The measurement of the nuclear compression constant $K = 9\rho^2 \left.\frac{\partial^2 W}{\partial \rho^2}\right|_{\rho=\rho_0, T=0}$ and the possibility of finding density isomers, i.e. secondary minima in the functional $W(\rho, T)$, are particularly fascinating and important opportunities.

Nucleus-nucleus collisions in the high-energy region > 100 MeV/N up to relativistic energies have – in the past – been studied using as projectiles fast nuclei from the cosmic radiation. Many of the experimental data have been obtained from measurements of star-events produced in nuclear emulsion as target and detector, where they could be observed in 4π-geometry.

A wide spectrum of energies and masses of the projectiles, and the mixture of different light and heavy nuclei in the target – the nuclear emulsion – have complicated the evaluation of those experiments and have restricted the informations available from them.

A new access to the investigation of high-energy nucleus-nucleus collisions has been opened with the availability of beams of heavy ions at fixed energies up to 2.1 GeV/N at the Bevatron accelerator of the LBL at Berkeley.

Using as target a new type of solid state particle track-detectors, developed at the University of Frankfurt [3–5], which consist of thin monocristalline layers of silverchloride only, we were able to confine the interactions of the heavy ion projectiles (^{16}O, ^{12}C or ^{4}He) on the two nuclides of the detector with medium

* This work was supported by the Bundesministerium für Forschung und Technologie (BMFT) and by the Gesellschaft für Schwerionenforschung (GSI). – Orally presented at the Bormio Winter Meeting (January 22, 1975), at the GSI-Seminar (February 4, 1975), and at the Users Meeting at the LBL, Berkeley (March 15, 1975).

** On leave of absence from Kyoto-Sangyo University, Kyoto, Japan.

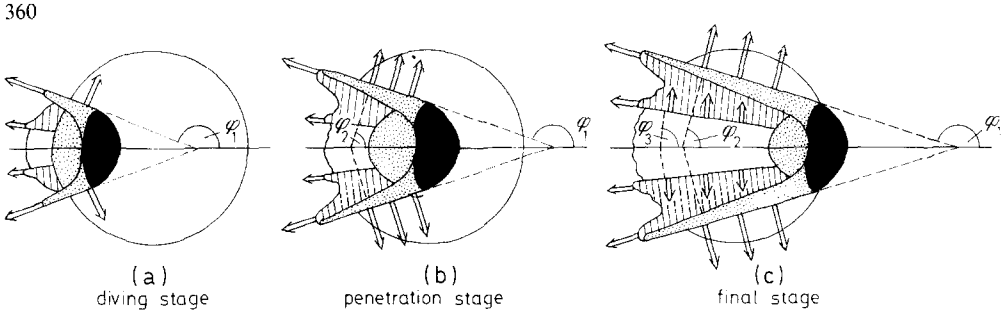

Fig. 1. The various stages of a central penetration of a light nucleus into a heavier one at high bombarding energies. The scattering of particles along the Mach shock front into the backward hemisphere occurs in the direction fixed by the angle φ_1. The main Mach shock front moves in the direction given by $\varphi_2 = \varphi_1 - 90°$. Further Mach shock fronts travel with lower density discontinuities indicated by φ_3. The head shock front (black area) has the highest density

masses, $_{47}$Ag and $_{17}$Cl. (A small amount of 0.5% $_{48}$Cd-doping may be accounted to the neighbouring Ag nuclide.) Assuming the cross sections for (O, Ag) or (O, Cl)-collisions resp., as proportional to $(R_{Ag}+R_O)^2$ and $(R_{Cl}+R_O)^2$ the ratio of interactions will be $\sigma_{Ag}/\sigma_{Cl}=1.62$, i.e. 62% of all collisions will occur at the silver nucleus.

These detectors have been irradiated at the LBL-accelerator with fast ions of oxygen at energies of 2.1, 0.87 GeV/N and carbon at 0.25 GeV/N and with He-ions at 0.87 GeV/N.* Evaluating these interactions which present themselves as star events in the volume of the detector in 4π-geometry, we were able to follow up trends in their appearance with the projectile energy.

Amongst other data we observed peaks in the angular distribution of the reaction products at forward and at backward angles, which, by following their position and their shift with the energy of the projectile, will be interpreted as signatures of nuclear shock waves.

The paper is arranged in the following way: In Sect. 2 the general concepts of shock waves and Mach shock waves are presented together with a discussion of the validity of hydrodynamics and thermodynamics. The third section contains the relativistic shock equations for an one-phase nucleonic gas and an isobaric gas. This is followed by the presentation of the experiment in Sect. 4, the interpretation of the various observations in Sect. 5, and the final outlook on some possibilities provided by shock waves for experimental investigation.

2. Shock Waves and Mach Cones

If the projectile nucleus with A_1 nucleons is rather small compared to the target nucleus with A_2 nucleons, the situation of a central relativistic collision can be schematically depicted as in Fig. 1, which shows three phases of interpenetration. In the first, the diving stage, the projectile enters the target with supersonic velocity and thus creates a high density shock denoted as *head shock*, which is strongest on the projectile's head and therefore penetrates faster along the incident trajectory through the larger nucleus.** Due to this shock. matter is expected to be pushed to the side and along the sidewards developing surface of the compression wave at angles φ_2 and $\varphi_1 = \varphi_2 + 90°$, where φ_2 characterizes the propagation of the Mach front. The flow of matter into backward angles is analogous to splashes occuring, when a fluid drop hits a fluid surface. When the shock front intersects the nuclear surface at positions φ_2 and φ_1, matter will be ejected because of the high pressure within the front.

In the penetrating stage the *Mach shock wave* becomes fully developed and propagates in the direction characterized by the angle φ_2 (Fig. 1). The occurrence of the Mach cone is possible because the density in the Mach shock wave is lower than the density in the head shock wave and therefore the velocity $(v_s)_{Hs}$ of the head shock wave is larger than the velocity $(v_s)_{Ms}$ of the Mach shock wave. Indeed, as shown in Fig. 5, the velocity of a shock front increases with the density in the shock zone: The higher the density, the larger the shock velocity v_s. Behind the projectile highly disturbed matter of lower density appears. This zone can be thought as a collapsing "drilled hole" or "dead water".

In the various high density zones the temperature T is rather high (we refer to Fig. 3). This makes the creation of nuclear isobars possible with densities determined

* We are greatly indebted to our colleagues at Berkeley, Dr. Grunder, F. Lothrop and Dr. Heckman, LBL, and Dr. Benton and Dr. Cruty, University of San Francisco, for their kind help.

** The rather sharp, experimentally observed Mach angles (see Fig. 9) and the very small recoil of the residual nucleus (see Table 1) indicate that the head shock wave is moving rather friction-free and compact through nuclear matter. The reason for that could be the occurrence of pion condensate ($\pi^+ - \pi^-$-dipole layer cloud). At present it cannot clearly be decided theoretically whether π^--mesons are also bound like the π^+, or whether they autoionize like positrons in overcritical fields. In the latter case one would expect the reaction $\pi^+ + n \to p$ to occur, thus leading to proton-rich (or neutron-poor)reaction products.

by the Boltzmann distribution

$$\rho_i = \frac{\tau_i\, e^{-E_i/T}}{\sum_{k=1}^{N} \tau_k\, e^{-E_k/T}}\, \rho \equiv \gamma_i \rho \tag{1}$$

where τ_i is the statistical weight and E_i the excitation energy of the i-th isobar; ρ denotes the total baryon density and ρ_1 the density of nucleons ($E_1 = 0$). Therefore, in violent shock waves large quantities of hot and highly isobaric matter should occur [1, 2, 8], which probably have quite different characteristics and behaviour as ground state matter. A thorough and detailed study of the shock phenomena, the emission of particles, the measurement of the temperature through evaporation spectra and of the production of isobars may answer some of these questions and deepen our understanding of baryonic matter. Particularly the structure of the fundamental energy density functional $W(\rho_i, T)$, which we will discuss in some approximation, can be investigated via the shock processes.* This includes the possible existence of *density isomers*.

The creation of isobars is also important in another respect, namely for the equilibrization of energy and hence for the validity of hydrodynamics and thermodynamics in nucleus-nucleus collisions. Indeed, the created N^* will immediately decay with a decay time of 10^{-24} sec, and emit pions which are reabsorbed by the neighbouring nucleons, i.e. $N^* \to N + \pi \to N^* \to \cdots$ (Ref. 9). The typical mean free path for pions in nuclear matter is

$$\lambda_\pi = \frac{1}{\sigma_\pi \rho} \approx 0.3\, \rho_0/\rho \text{ fm} \tag{2}$$

where we use $\sigma_\pi \approx 200$ mb. This pion wave moves through the nucleus and helps indeed for equilibrization. At the nuclear surface, the pion emission can be expected to be more or less thermal except for those pions carried in the various shock waves.

The typical mean free path of nucleons is determined by

$$\lambda_N = \frac{1}{\sigma_N \rho} \simeq 1.4\, \rho_0/\rho \text{ fm} \tag{3}$$

where $\sigma_N \approx 40$ mb is the free elastic nucleon-nucleon cross section. This is important for the initial development of the shock. Because of the relativistic shrinking one initially has for high energetic collisions:

$$\frac{\rho}{\rho_0} = \frac{1}{\sqrt{1-\beta^2}} = 1 + \frac{E_{\text{kin}}}{M_0 c^2}.$$

Therefore, the free path $\lambda_N = 1.4/(1 + E_{\text{kin}}/M_0 c^2)^{-1}$ fm is small compared to the dimensions of the target nucleus. At lower energies the relativistic increase of the density due to shrinking decreases, whereas inversely the nucleon-nucleon cross section increases. Therefore, the conclusion remains valid. This should be sufficient to initiate shocks even at energies of 2 GeV/N. After that occurred, the density ρ becomes even higher and the inelastic processes described above set in, so that hydrodynamics has validity [1, 2, 10]. Hence even a certain transparency of nuclear matter should not inhibit the formation of shock waves, except if $\sigma_N(E)$ drops at ultrahigh energies faster than $1/\gamma = \sqrt{1-\beta^2}$.

The Mach cone should be observed in the direction φ_2 given by

$$\cos\varphi_2 = (v_s)_{Ms}/(v_s)_{Hs}. \tag{4}$$

The velocity $(v_s)_{Hs}$ of the head shock wave is related to the kinetic energy of the projectile and is determined in Sect. 5.

Mach shock waves do also occur for noncentral collisions as long as the overlap of the two colliding nuclei is not too small and the interaction violently enough. In these cases the Mach front still propagates in the direction φ_2. Since collisions will occur equally often for all azimutal angles around the central collision axis, the Mach shock cone will also be visible in the statistical ensemble of all collisions which is demonstrated in Fig. 2. In this case, also the shock front in the projectile is of some importance. The noncentral collisions can be experimentally distinguished from the central collisions in track detectors (see Sect. 4 and Fig. 12).

The particles and clusters finally ejected from the Mach shock wave at the nuclear surface will have a maximum velocity v_f which is the velocity of matter flow in the compressed zone (see Eq. (23)). Hence their maximum kinetic energies

$$E_{\text{kin}} = Mc^2 \left(\frac{1}{\sqrt{1-(v_f/c)^2}} - 1 \right) \tag{5}$$

are proportional to their masses. This can serve in future as a further experimental check on the shock waves: The particles ejected under the shock angle should fulfil this relation; we note, however, that the density in the Mach shock decreases behind its front which leads to a *velocity dispersion* and hence also to a directed emission of slower particles (see the schematic Fig. 8).

The distribution of the particles and the fragments in the Mach cone will obtain an angular spread $\Delta\varphi_2$ due to the zero point motion $E_{\text{fermi}} \approx 30$ MeV and due to

* In the introduction we spoke of $W(\rho, T)$ but learn now that in fact it is a functional depending on all ρ_i, i.e. $W(\rho_i, T)$. Nevertheless, for simplicity reasons and also because it is a good approximation near $T = 0$, we will use $W(\rho, T)$ in some parts of our discussion later on.

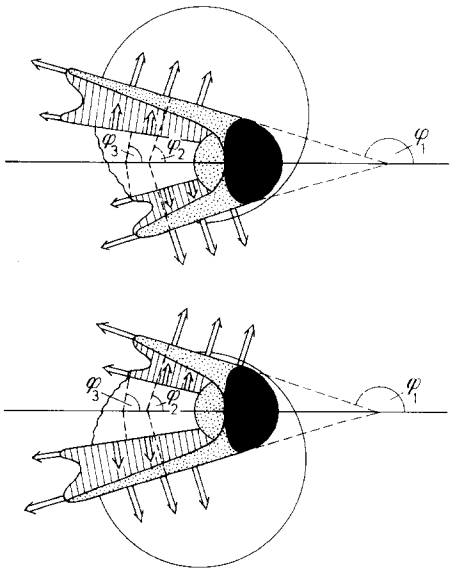

Fig. 2. Noncentral collision of a light nucleus with a heavier one. The resulting angles of the Mach fronts are expected to be the same as for the central collision discussed in Fig. 1

the thermal energy $E_{\text{therm}} \approx 50$ MeV. The value of the thermal energy depends on the density in the Mach shock front and can eventually serve for its experimental observation. $\Delta\varphi_2$ is determined via $\Delta v_{Ms}^2 = 2(E_{\text{Fermi}} + E_{\text{therm}})/M_0$ by

$$\Delta\varphi_2 = \left| \arccos\left[\frac{1}{v_{Hs}}\left(v_{Ms}^2 + \left(1 - \frac{v_{Ms}^2}{c^2}\right)\Delta v_{Ms}^2\right)^{1/2}\right] - \varphi_2 \right|$$
$$\approx 5 - 15°. \tag{6}$$

3. Relativistic Shock Equations

3.1. One-Phase Nucleon Gas

First for simplicity we consider a one-phase gas of nucleons with density ρ, i.e. we neglect the production of isobars [2, 8]. Basic for its behaviour is the energy per nucleon $W(\rho, T)$ as a function of ρ and T, for which we use the ansatz

$$W(\rho, T) = \frac{e(\rho, T)}{\rho} = M_0 c^2 - \tilde{W}_0$$
$$+ \frac{C}{2\rho\rho_0}(\rho - \rho_0)^2 + \frac{e_T(\rho, T)}{\rho} \tag{7}$$

where $\tilde{W}_0 \approx 16$ MeV is the binding energy per nucleon in the ground state of nuclear matter ($T = 0$). The third term describes the compression energy per particle, i.e. an expansion of $W(\rho, T)$ around $\rho = \rho_0$. C is related to the compression constant K by $K = 9\,C$. e_T denotes a general function for the volume density of the thermal energy, which has to obey the only requirement that the partial pressure p_{therm} is connected with the thermal energy per particle $E_{\text{therm}} = e_T/\rho$ via the relation

$$p_{\text{therm}} = \alpha\, e_T(\rho, T)$$

where α is a constant factor. The total pressure is given by

$$p = p_{\text{comp}} + p_{\text{therm}} = \rho^2 \left.\frac{\partial W}{\partial \rho}\right|_{\text{const entropy}}$$
$$= \frac{C}{2\rho_0}(\rho^2 - \rho_0^2) + \alpha\, e_T(\rho, T). \tag{8}$$

This relation should be illustrated by two examples: For the ideal gas it follows from $pV = NkT$ that $p_{\text{therm}} = \rho kT$ and, therefore, $E_{\text{therm}} = \frac{3}{2}kT = e_T/\rho$, which in turn gives $p_{\text{therm}} = \frac{2}{3}e_T$. Hence we find $\alpha = \frac{2}{3}$ in this case. The same is also true for the Fermi gas, for which

$$E_{\text{therm}} = \frac{1}{2}\beta T^2 \rho^{-2/3} = \frac{e_T}{\rho} \quad \text{with } \beta = \left(\frac{2\pi}{3}\right)^{2/3} \frac{M_0 c^2}{(\hbar c)^2}$$

holds. For the Fermi gas the pressure is calculated to be $p = \frac{C}{2\rho_0}(\rho^2 - \rho_0^2) + \frac{2}{3}e_T$, which has again the form (8).

At the shock front the continuity of energy and momentum flux must be assured. It yields the relativistic Rankine equation which reads with the specific enthalpy $i = e + p$ (Refs. 11, 12)

$$\frac{i_0^2}{\rho_0^2} - \frac{i^2}{\rho^2} + (p - p_0)\cdot\left(\frac{i_0}{\rho_0^2} + \frac{i}{\rho^2}\right) = 0. \tag{9}$$

The quantities on both sides of the shock front are distinguished by the index 0 and no index, respectively. Inserting (7) and (8) into (9) yields a relation for the energy density as a function of ρ:

$$e_T = \frac{a}{2} + \sqrt{\frac{a^2}{4} + b}$$

$$a = \frac{1}{(1+\alpha)\rho_0}\left[(M_0 c^2 - \tilde{W}_0)(\alpha\rho^2 - (\alpha+2)\rho\rho_0)\right.$$
$$\left. - \frac{C}{2}(\rho - \rho_0)(3\rho - \rho_0 + \alpha(\rho - \rho_0))\right]$$

$$b = \frac{C}{2}\frac{\rho}{(1+\alpha)\rho_0^2}(\rho - \rho_0)^3 (M_0 c^2 - \tilde{W}_0 - C). \tag{10}$$

This in turn yields for any $e_T(\rho, T)$ the temperature T in the shock front as a function of the shock density. In Fig. 3 the temperature $T(\rho)$ is shown for various values of compressibility: The thermal energy per nucleon $E_{\text{therm}}(\rho)$ can be seen in Fig. 4a. Obviously there occurs no limiting density as in the nonrelativistic theory [1, 2], even though the shock equation (9) reduces in the limit $M_0 c^2 \to \infty$ to the nonrelativistic

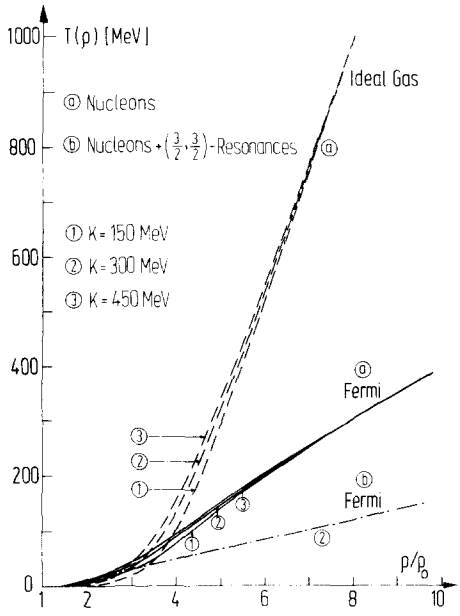

Fig. 3. The temperature $T(kT$ in MeV) as function of the density following from the relativistic Rankine equation (9), for the ideal gas (dashed lines), and the Fermi gas ansatz (full lines) for various compressibilities. The dotted-dashed line is the temperature T for the Fermi gas including the $(\frac{3}{2}, \frac{3}{2})$-resonance for $K = 300$ MeV

Rankine-Hugoniot equation [1, 2, 13, 14]

$$2(W - W_0) + (p + p_0) \cdot \left(\frac{1}{\rho} - \frac{1}{\rho_0}\right) = 0 \tag{11}$$

which has a pole at $\rho = 4\rho_0$ for $\alpha = \frac{2}{3}$ (Refs. 1, 2). The compression energy per nucleon, given by the third term of Eq. (7) is graphically depicted in Fig. 4b and the excitation energy per nucleon in Fig. 4c.

The above mentioned continuity equations at the shock front lead also to the shock velocity v_s relative to the resting fluid characterized by $p_0 = 0$ and $W_0 = e_0/\rho_0 = W(\rho_0, 0)$. It is given by

$$\frac{v_s}{c} = \sqrt{\frac{p \cdot e}{(e - e_0)(e_0 + p)}}$$

$$= \sqrt{\frac{p \cdot W(\rho, T) \cdot p}{(W(\rho, T) \cdot \rho - W(\rho_0, 0) \cdot \rho_0) \cdot (W(\rho_0, 0) \cdot \rho_0 + p)}}. \tag{12}$$

With Eq. (10) the shock velocity can be expressed as a function of ρ only and approximates $v_s \to c$ for $\rho/\rho_0 \gg 1$. It is depicted in Fig. 5 for various compression constants and equations of state, i.e. values of α.

3.2. *Isobaric Gas*

The complex situation in a relativistic nucleus-nucleus collision is more properly described by a many-phase isobaric gas, which allows for the excitation of the nucleons to their various excited states. Assuming a Boltzmann distribution, the baryonic densities of the various phases are given by Eq. (1). In addition one should also treat the pionic phase which, however,

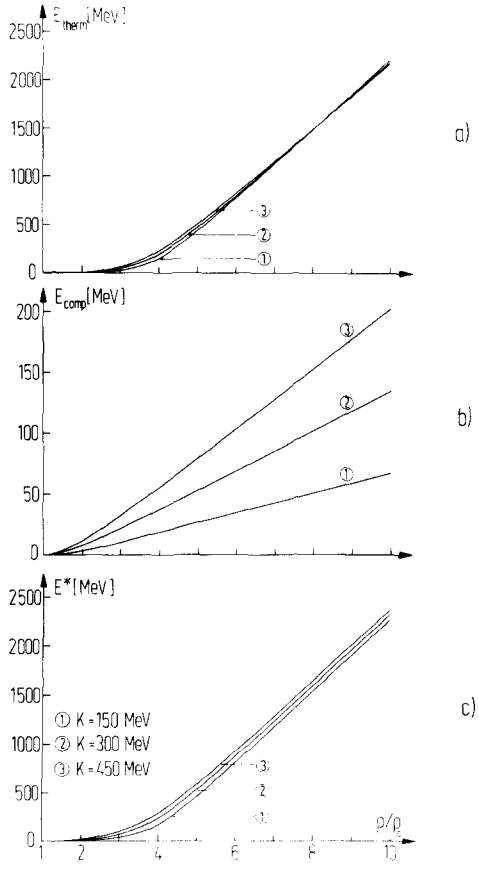

Fig. 4. The thermal energy, the compression energy and the total excitation energy per nucleon as function of the density for $\alpha = \frac{2}{3}$. The thermal energy is calculated with Eq. (10). The total excitation energy is given by the sum of the thermal energy and the compression energy

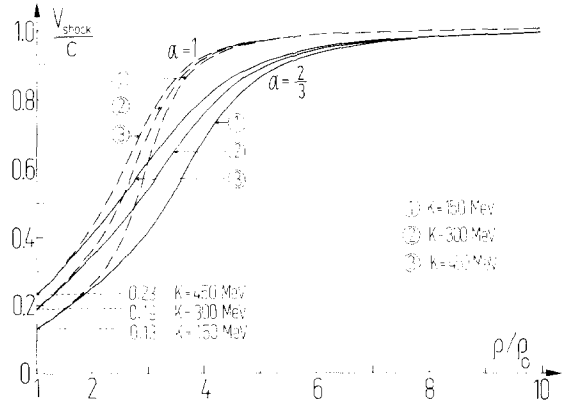

Fig. 5. The velocity of the shock front according to Eq. (12) as function of the density ρ/ρ_0 for $\alpha = \frac{2}{3}$, 1 and for various compression constants K. The velocity of the first sound in nuclear matter is given by the value of v_s at $\rho/\rho_0 = 1$

we disregard at present to simplify the treatment.* We assume also the same velocity field for all baryonic phases and, furthermore, that the total energy density of the many-phase baryonic gas can solely be expressed by the total density ρ and a common temperature T. Eq. (7) is accordingly changed into

$$W(\rho, T)=\frac{e(\rho, T)}{\rho}$$

$$=M_0 c^2-\tilde{W}_0+\frac{C}{2\rho\rho_0}(\rho-\rho_0)^2+\frac{e_T(\rho, T)}{\rho} \quad (13)$$

where

$$\frac{e_T}{\rho}=\sum_{i=1}^{N}\left(K_i\frac{T^n}{\rho_i^{\alpha(n-1)}}+(M_i-M_0)c^2\right)\gamma_i. \quad (14)$$

The nucleonic phase is denoted by $i=1$. $M_1=M_0$ is the mass of the nucleon and the γ_i are defined in Eq. (1). Here, $n=1$ describes the ideal gas and $n=2$, $\alpha=2/3$ the Fermi gas. The K_i are certain constants, which are given e.g. for the Fermi gas by

$$K_i\equiv\frac{\beta_i}{2}=\frac{1}{2}\left(\frac{2\tau_i\pi}{3}\right)^{2/3}\frac{M_i c^2}{(\hbar c)^2}.$$

The pressure results from $(n\neq 1)$:

$$p=-\rho^2 T\int_0^T\frac{1}{T^2}\left(\frac{\partial W}{\partial\rho}\right)_T dT=\frac{C}{2\rho_0}(\rho^2-\rho_0^2)$$

$$+\frac{\alpha T}{\rho^{\alpha(n-1)-1}}\int_0^T(n-1)\cdot T^{n-2}\sum_{i=1}^{N}\frac{K_i}{\gamma_i^{\alpha(n-1)-1}}dT. \quad (15)$$

For $N=1$, i.e. for the one-phase nucleonic gas, we have $\gamma_1=1$ and Eq. (15) becomes Eq. (8). Under the assumptions outlined above, the relativistic shock equation is exactly the same as in Eq. (9). This is rather obvious, because the shock equation is a consequence of momentum, energy and baryonic number conservation across the shock front. Assuming that before the shock front $W_0=W(\rho_0, T=0)=M_0 c^2-\tilde{W}_0$ and $p_0=0$, it can be written in the following more explicit form

$$0=2(W-W_0)+p\left(\frac{1}{\rho}-\frac{1}{\rho_0}\right)+p\cdot\left(\frac{1}{\rho}+\frac{1}{\rho_0}\right)\cdot\frac{W-W_0}{W+W_0}, \quad (16)$$

which shows the relativistic addition (third term) to the non-relativistic Rankine equation (first two terms, see Eq. (11)). Its solution can only be obtained numerically. The resulting functional $T=T(\rho)$ is also shown in Fig. 3 for an isobaric Fermi gas including the nucleon- and the 3/2−3/2 resonance-phases only. The thermal energy which contains also the internal energy of the isobars is compared in Fig. 6 with the one-phase approximation of Fig. 4 and shows a strong increase with temperature. Also the dependence of the shock velocity on the total baryonic matter density ρ/ρ_0 is changed due to isobar degrees of freedom as shown in Fig. 7.

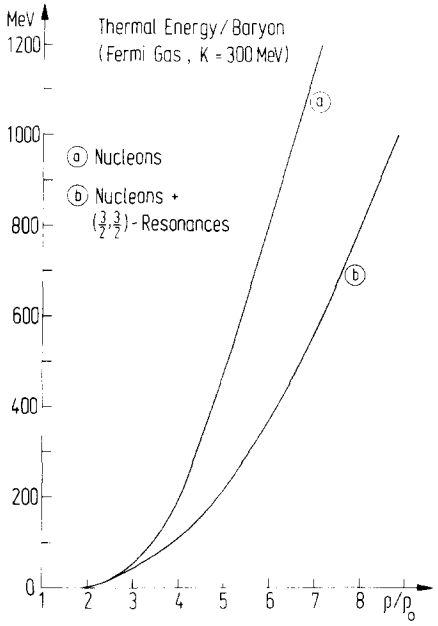

Fig. 6. Thermal energy per baryon as function of the isobaric density for the Fermi gas ansatz (Eq. (14) with $n=2$, $\alpha=\frac{2}{3}$). Only nucleons and $(\frac{3}{2}, \frac{3}{2})$-resonances are included in the calculation. For comparison the thermal energy for the one-phase gas consisting of nucleons only is shown. The last curve is also drawn in Fig. 4a

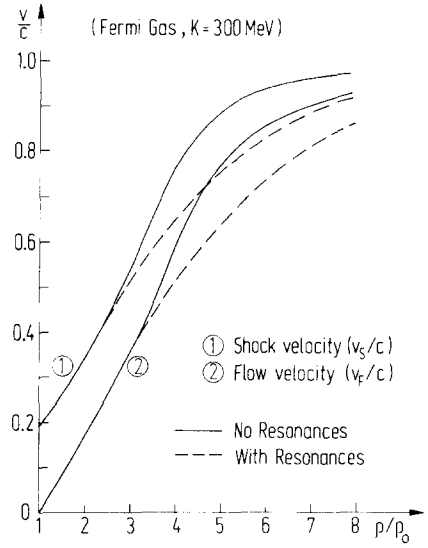

Fig. 7. The velocity of the shock front and the velocity of matter, flowing in the compressed region behind the shock front (Eq. (23)), for $K=300$ MeV for the nucleon gas and the two-component gas consisting of nucleons and $(\frac{3}{2}, \frac{3}{2})$-resonances as function of the density. It should be noted that for smaller densities only a few $(\frac{3}{2}, \frac{3}{2})$-resonances are excited and both curves do not differ appreciably

* Since the pion mass is $M_\pi\approx\frac{1}{7}M_0$ the velocity field of the pionic gas is considerably different from the baryonic one and the above simplified treatment would need major modifications.

4. The Experiment

4.1. The Detectors and Their Evaluation

The detectors consist of monocrystalline sheets of 150 to 300 microns thickness of pure silverchloride (density $\rho = 5.6\ \mathrm{gcm}^{-3}$), doped with 200 to 8000 ppm of Cd, depending on the sensitivity desired.

The detector sheets used in these experiments, were supported by thin plates of quarzglass with dimensions of 1.5 times 2.5 cm^2, in order to prevent mechanical distortions by the handling procedures. They also can be used as large free foils and mounted as stacks.

Based on a similar fundamental process of the formation of particle tracks as in the nuclear emulsion, they possess, besides the more simple and homogeneous structure compared to the latter, several interesting particular properties [4–6]. We are giving here some details which are relevant for the experiment.

The tracks of charged particles in the detectors are made visible – developed – simply by irradiation with ultraviolet light ($\lambda \sim 406$ nm) after the exposure to particles; deformations and shrinkage by the processing are thus excluded. Undeveloped tracks of particles are quickly fading, unless they are not stabilized during the particle exposure by inactinic, for instance yellow light [5]; kept in darkness, the detectors remain free of background-tracks.

The detectors have been exposed to the heavy ion beam – partly parallely partly perpendicularly to the detectors surface – with about 10^5 particles/cm^2.

The star-events observed were evaluated by means of a special electronic video-amplifier device, a modified Quantimet 720 (Fa. Imanco) [5].

High precision and reproducibility in the determination of track coordinates – eliminating subjective parameters – are achievable by the following means:

a) focussing of the microscopic image of the track on the video-screen, or, if necessary, in a nonsubjective way by determining electronically the depth position of the steepest lateral density profile $O(r)$ of the track;

b) electronic positioning of the x, y coordinates of the scanning field (the smallest corresponding to 0.05×0.05 microns at the detector site) combined with an electronic movement of the stage;

c) electronic measurement of the dip-coordinate z (± 0.1 micron).

The determination of the lateral density profile of the track-image projected on the video-amplifier cathode (with 20 picture-points per micron in the lateral dimension r of the track at the detector site) permits to calibrate the ionization of the particle.

Corresponding to the doping concentration of 5000 ppm Cd, the detectors used in our experiment had a sensitivity threshold: If we admit "grained"

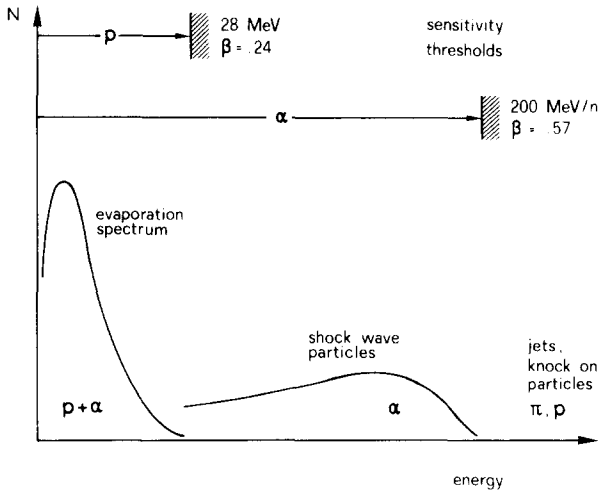

Fig. 8. In the upper half of the figure the sensitivity thresholds of the AgCl-detectors for protons (28 MeV) and He-particles (200 MeV/N) are shown. Below there are drawn the schematic spectral ranges of the evaporation component (p, d, α-particles), of the shock wave component and of the knock-on and cascade particles

tracks – in the terminology of nuclear emulsion people: grey and white tracks which also occur in AgCl-crystals – and if we fix the threshold of recognizability of a track at the opacity $O = 0.2$,* the threshold will be given by a linear energy transfer (LET)

$$\left(\frac{dE}{dx}\right)_{\mathrm{thr}} = 10.7 \frac{\mathrm{MeV}}{\mathrm{g\,cm}^{-2}} \sim 6 \frac{\mathrm{keV}}{\mathrm{micron}} \sim 8.5 \left(\frac{dE}{dx}\right)_{\mathrm{min.}Z=1} \tag{17}$$

with corresponding energies of

$E \sim 28$ MeV for protons, $\beta = 0.24$

~ 4.4 MeV for π-mesons,

~ 200 MeV/N for α-particles, $\beta = 0.57$

Thus the particles recorded in our detectors roughly correspond to the group of black prongs in K5-emulsion. We should keep in mind that α-particles up to $E = 200$ MeV/N are falling into this group; they are of particular interest in the context of shock waves, whereas singly charged particles of corresponding LET, π-mesons and protons, are low-energetic only; the latter are belonging to the so-called evaporation spectrum, which occurs in the final phase of high energy nuclear interactions (see Fig. 8).

4.2. Angular Distributions and their Components

We have, first of all, determined the angular distributions of all particles emitted from stars with $\geqq 3$ prongs.

* Following Barkas [7], two tenth of a unit of length of a track are covered by silver.

We could disregard their mass and charge for the following reasons:

Nucleus-nucleus collisions in the energy range considered, may be regarded as a superposition of different mechanisms: The incoming projectile represents a bulk of nucleons which make nucleon-nucleon interactions within the target nucleus. On the one hand they are creating knock-on particles and pion-jets of higher energy emitted mainly in forward angles in the lab-system and followed probably by cascade processes to a certain extent. On the other hand they are preparing the shock wave mechanism which we are discussing.

After these fast processes the excited residual nucleus comes to a gliding thermal equilibrium and deexcites by evaporating particles of low energies $\leqq 30$ MeV with a temperature spectrum: protons and α-particles mainly; a small amount consists of fragments and clusters.

We are interested in the intermediate stage, where cascades and compression waves are expected to develop. Following the schematic Fig. 8 the sensitivity cut-off of our detectors excludes the fast, mainly forwardly directed particles of the jet and knock-on group, except heavier fragments with $Z>3$, such as B, C, N, O; these, however, following recent results of the Heckman group at Berkeley [17], are also mostly emitted into small forward angles with low transverse momentum. At larger angles we are observing the evaporation component and He-particles of higher energies up to 200 MeV/N, which belong to the interesting group in the range of Mach shock velocities $(v_s)_{Ms}<0.6\,c$ (Table 2).

This argumentation is supported by the results of earlier work, in particular by Otterlund *et al.* [15, 16]: in stars produced in nuclear emulsion by nuclei of the cosmic radiation with energies > 100 MeV/N they find among the outcoming particles tracks of He-particles with energies above 30 MeV up to 200 MeV, – predominantly from larger stars (>8 prongs)–, which cannot be attributed – under reasonable assumptions – to the evaporation component.

The angular distributions obtained from collisions of ^{16}O-ions at 2.1 and 0.87 GeV/N and of ^{12}C-ions at 0.25 GeV/N with the nuclides Ag and Cl are depicted in Fig. 9. The left side gives the measured histogram, the right side the distribution after subtracting the calculated evaporation spectrum. The error bars are marking the peaks, which we attribute to hydrodynamic shock wave effects.

It may be noticed that besides the first peak in forward direction a satellite peak in backward direction appears, which is correlated to the first by a shift of 90°. We assign it to the backward "splashing tide wave" which is expected to occur at the discontinuity at the intersection of the shock front plane with the surface of the nucleus (Fig. 1).

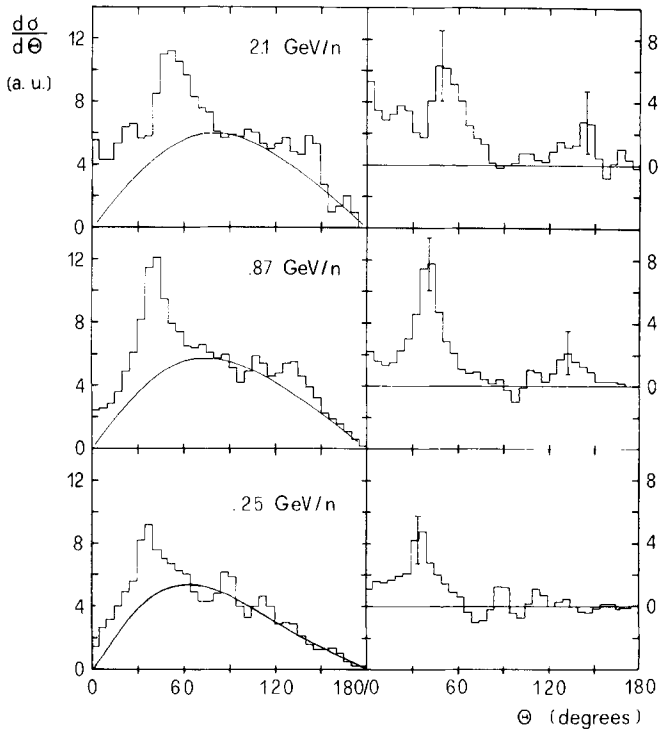

Fig. 9. Left hand side: Angular distributions $d\sigma/d\theta$ in arb. units of particles from stars at Ag and Cl nuclei, with different projectiles and energies; full line: calculated evaporation component

^{16}O at 2.1 and 0.87 GeV/N, stars >3 prongs

^{12}C at 0.25 GeV/N, stars $\leqq$ 13 prongs

ordinate: overlapping means

$1/4(f_{\theta-\Delta\theta}+2f_{\theta}+f_{\theta+\Delta\theta})$

abscissa: $\Delta\theta$ in 5 degrees.

Right hand side: remaining component after subtraction of the evaporation component (see text).

Error bars: σ_m (peak minus evaporation)

For comparison, in Fig. 10 angular distributions are depicted for ^{4}He and ^{16}O ions as projectiles at 0.87 GeV/N. In both cases the peaks appear at about the same angles, but with reduced height for He-particles (see also Note Added in Proof, page 371).

The number of particles and the energy spectrum of the evaporation component has been calculated following Le Couteur [18]. The angular distribution which is isotropic in the c.m.-system has to be shifted in forward direction as a consequence of the forward velocity (β_{res}) of the evaporating residual nucleus. We have to consider the following relations between the excitation energy U of the evaporating nucleus, its temperature T, the energy distribution $n(E)\,dE$ and the mean number of evaporating particles per star-event $\bar{N}_{evap}$. We are including protons, deuterons and

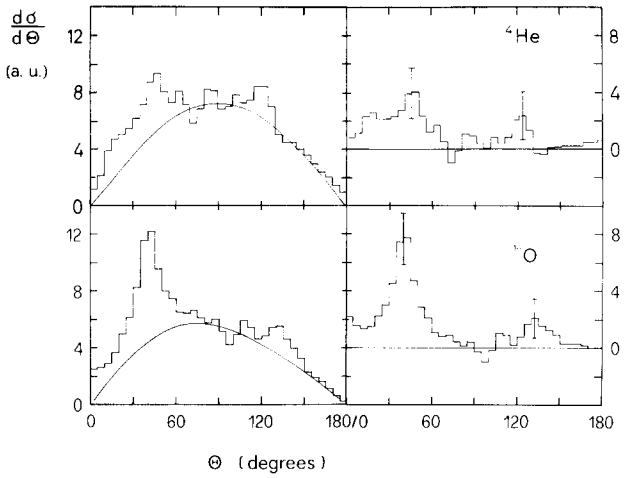

Fig. 10. Comparison of two angular distributions, plotted as in Fig. 9 for ^{16}O and ^{4}He as projectiles at energies of 0.87 GeV/N

α-particles with the ratio given by Le Couteur's theory. The excitation energy

$$U = a\,T^2 \cdot A \qquad a = 0.1,\ A = \text{mass number} \tag{18}$$

leads to $\bar{N}_{evap}(T)$. From the evaporation spectrum

$$n(E)\,dE = f(T, V_B), \qquad (V_B = \text{Coulomb barrier}) \tag{19}$$

follows a mean energy per evaporated particle

$$\bar{E}_{evap}(T, V_B) \quad \text{or} \quad \bar{\beta}_{evap}(T).$$

We have fitted the angular distribution of the evaporation component to the shape of the measured angular distributions (Fig. 9 and 10) at large angles $\theta > 130°$ and around $\theta = 90°$ where no hydrodynamic effects are expected. The fitted parameters are $\bar{N}_{evap}$ and β_{res}/β_{evap}, which are correlated by Eq. (18) and (19). The particles, remaining after subtraction of the evaporation component – right side of Figs. 9 and 10 – are due to the fast processes mentioned above, for instance shock wave effects.

Table 1 lists the data used for the calculation of the fitted evaporation curves. The Coulomb-barrier is taken as $V_B = 0$. Looking at the values of β_{res}, the momentum transfered to the residual evaporating nucleus occurs to increase with decreasing energy of the projectile: the collision mechanism becomes more frictional. As expected the momentum transfered by He-projectiles is much smaller.

Table 1. Evaporation data, used for the calculation of the curves in Figs. 9 and 10, averaged for Ag and Cl; $\bar{U}$ mean excitation energy; β_{res} velocity of the evaporating residual nucleus; mean number of prongs: $\bar{N}_h$ per star, $\bar{N}_{evap}$ evaporating particles per star

Projectile energy (GeV/N)		$\bar{U}$ (MeV)	β_{res}	$\bar{N}_h$	$\bar{N}_{evap}$	$\bar{N}_h - \bar{N}_{evap}$
^{16}O	2.1	210	0.02	8.2	5.6	2.6
	0.87	305	0.03	10.2	7.1	3.1
^{12}C	0.25	255	0.06	8.0	6.5	1.5
^{4}He	0.87	295	<0.01	8.8	7.4	1.4

We assign to the peaks Gaussian-like shapes; the errors, represented by bars in Figs. 9 and 10, correspond to the mean standard deviation σ_m of the difference d = peak-evaporation. For the forward peaks we find

$$\frac{d}{\sigma_m} = 2.7 \text{ for } 2.1 \text{ GeV/N } ^{16}O$$
$$= 4.4 \text{ for } 0.87 \text{ GeV/N } ^{16}O$$
$$= 3.2 \text{ for } 0.25 \text{ GeV/N } ^{12}C.$$

The backward satellites shifted by 90°, are not significant, regarded as isolated peaks. Their correlation to forward peaks, and their occurrence with three projectils are, however, supporting their significance.

We have checked alternatives to the shock wave explanation:

One of the hypotheses to be considered with regard to the energy range covered by the detector sensitivity was that of a simple evaporation mechanism. Using the free parameters $\bar{N}_{evap}$, the mean number of evaporating particles per star-event, and β_{evap}/β_{res}, the mean velocities of the evaporating particles and of the residual nucleus, we have adjusted evaporation curves to the histograms by least square fits. They could be rejected by χ^2-tests; in the case of oxygen-projectiles of 0.87 GeV/N at the 0.01 level. Besides this statistical argument, the fit requires a rather high number of $\bar{N}_{evap} = 9.6$ compared to the whole mean number $\bar{N}_h = 10.2$ prongs per star-event, and $\beta_{res} \sim 0.08$; they are in contradiction to known data [15, 16] and to our data which we finally elaborated (comp. Table 2) for the calculated curves in Fig. 9.

The possible objection that a kinematic cut-off of the angular distributions towards smaller forward angles or faster particles due to the sensitivity threshold of our detectors, might simulate the peaks, could be ruled out. We have calculated the angles under which protons are scattered with 28 MeV, and α-particles with 200 MeV/N by the impact with nucleons or clusters from projectiles of various energies (Fig. 11). The comparison with the experimentally observed peaks shows that the latter cannot be caused by a kinematic cut-off.

In order to examine the influence of the different masses of the target nuclei Ag and Cl onto the position of the observed peaks, we have compared the angular distributions of particles from all stars ($\geqq 3$ prongs) with those from small stars (3–6 prongs) and from large stars (> 13–30 prongs); the latter are ascribed to collisions with Ag. With ^{16}O-projectiles at 0.87 GeV/N

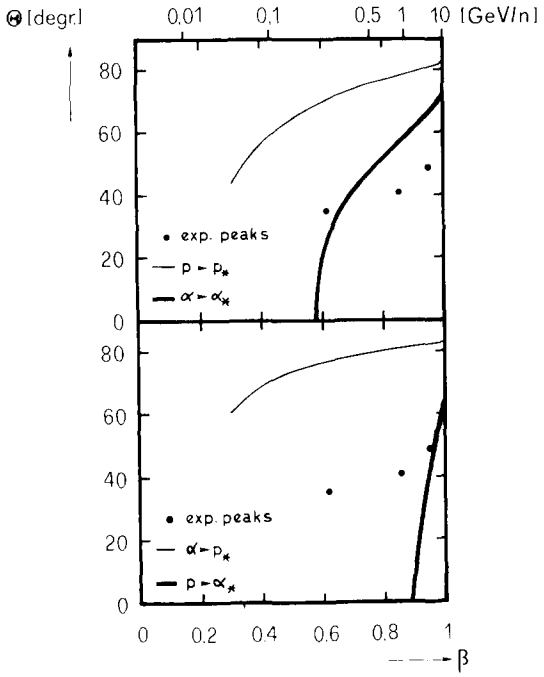

Fig. 11. Calculated angles under which protons of 28 MeV (p_*) and α-particles of 200 MeV/N (α_*) are scattered in collisions with nucleons and α-particles of the projectile at different projectile energies

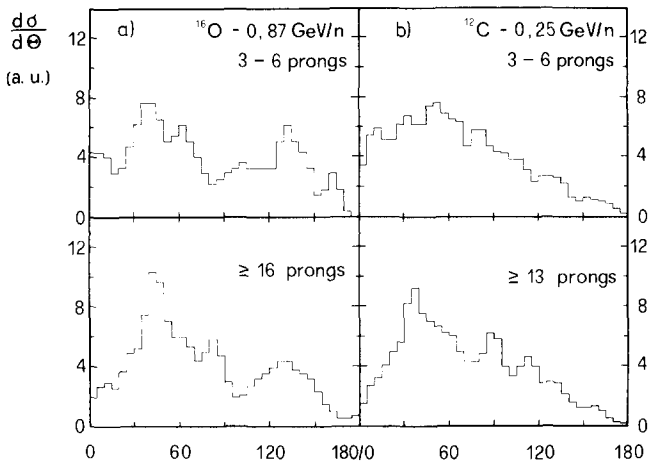

Fig. 12. Angular distributions of particles from stars produced at Ag and Cl nuclei, for small stars (3–6 prongs) and for large stars (>13 prongs) by (a) ^{16}O at 0.87 GeV/N, (b) ^{12}C at 0.25 GeV/N

the position of the peak does not remarkably change (Fig. 12a). It is, however, smeared out and disappearing at 0.25 GeV/N with small stars (Fig. 12b). This is well fitting with findings of Otterlund [16] that the α-particles observed with energies above the evaporation spectrum did not occur in small stars.

If we observe large and symmetrical stars, which can be discriminated easily (and only) in track-detector experiments, we obviously exclude strongly peripheral collisions, which at lower energies, where the mean star size is smaller, are covering the shock wave effects.

A more detailed examination of these questions will be given in the diploma thesis by H.G. Baumgardt [21]. We often observe tracks of narrow pairs or triples of particles emerging from the star-events; they could be due to clusters formed in the compression zone and decaying at the nuclear surface in a collective motion.

5. Interpretation of the Experiment

The angular distributions of the fragment tracks observed in the star-events show indeed the theoretically predicted peak structure: For ^{16}O or ^{12}C ions respectively these peaks (first peak and its satellite) are listed for various projectile energies in Table 2.

From the 0.25 GeV/N data we deduce the Mach shock velocity $(v_s)_{Ms} = 0.49c$. The density ρ needed to calculate v_s with Eq. (12) can be obtained in a dynamical nonrelativistic calculation as described in Refs. 1, 2. It depends on the compression constant K. To reproduce approximately the 0.25 GeV/N-data we take $K = 300$ MeV. This compression constant yields $c_s = \sqrt{C/M} = \frac{1}{3}\sqrt{K/M} = 0.19c$ for the velocity of first sound. With that the dynamical nonrelativistic calculation predicts the Mach shock densities as function of the projectile energy per particle as shown by the full curves in Fig. 14. The Mach shock densities can also be deduced from the experimental Mach angles φ_2. For that we first calculate the Mach shock velocity $(v_s)_{Ms} = \cos\varphi_2 \cdot (v_s)_{Hs}$ and then deduce the Mach shock densities $(\rho/\rho_0)_{Ms}$ from the curves in Fig. 7. The connection of the head shock velocity $(v_s)_{Hs}$ with the projectile energy is discussed in Eqs. (20)–(23) (see also Fig. 13). The resulting densities $(\rho/\rho_0)_{Ms}$ are listed in Table 2 and shown in Fig. 14.

Obviously there is qualitative agreement in Fig. 14, but it should be remarked that the high energy data are sensitive to the relativistic effects, the density functional $W(\rho, T)$ and in particular to the temperature energy term $e_T(\rho, T)$. A possible structure in $W(\rho, T)$ for densities $\rho > \rho_0$ (density isomer) influences the theoretical behaviour of $(\rho/\rho_0)_{Ms}$ in Fig. 14 significantly.* The fact that the Mach shock velocity is practically the same for projectile energies ≧870 MeV indicates, that the Mach shock densities for these energies are the same, which is a surprising, but not unphysical

* We note, that density isomers in $W(\rho, T)$ would lead to regions of negative pressure $p = \rho^2 \frac{\partial W}{\partial \rho}$.

One can therefore expect that the shock wave phenomena will disappear in that region of the density or projectile energy – which both are correlated – where the isomer occurs. Even though the temperature will smear out this effect somewhat, it can eventually be used as a signature in the search for density isomers.

Table 2. The experimental angles for the forward and satellite peak, the density and the velocities in the Mach shock wave and head shock wave. The quantities ρ/ρ_0, v_s and v_f are calculated assuming an isobaric Fermi gas consisting of nucleons and $(\frac{3}{2},\frac{3}{2})$-resonances. The compression constant is taken as $K=300$ MeV. We obtain the head shock density $(\rho/\rho_0)_{Hs}$ from Fig. 13 and then, the velocities $(v_s)_{Hs}$, $(v_f)_{Hs}$ from Fig. 7. The Mach shock velocity $(v_s)_{Ms}$ is calculated by using the experimental angle φ_2: $(v_s)_{Ms}=\cos\varphi_2\cdot(v_s)_{Hs}$. With $(v_s)_{Ms}$ the density $(\rho/\rho_0)_{Ms}$ and velocity $(v_f)_{Ms}$ are obtained from Fig. 7

Projectile	Projectile energy	$\beta_{proj}=v_{proj}/c$	Forward peak (exp.)	Satellite peak (exp.)	Mach shock wave					Head shock wave				
					$(\rho/\rho_0)_{Ms}$	$(v_s/c)_{Ms}$	$(v_s)_{Ms}/v_{proj.}$	$(v_f/c)_{Ms}$	$(v_f)_{Ms}/v_{proj.}$	$(\rho/\rho_0)_{Hs}$	$(v_s/c)_{Hs}$	$(v_s)_{Hs}/v_{proj.}$	$(v_f/c)_{Hs}$	$(v_f)_{Hs}/v_{proj.}$
	GeV		φ_2	φ_1										
^{16}O	2.1	0.95	51°	144°	3.4	0.57	0.60	0.42	0.44	7.4	0.90	0.95	0.84	0.88
$^{16}O, \alpha$	0.87	0.86	43°	137°	3.5	0.58	0.68	0.44	0.51	5.6	0.80	0.93	0.69	0.81
^{12}C	0.25	0.61	36°		2.9	0.49	0.80	0.34	0.55	3.7	0.61	0.99	0.47	0.77

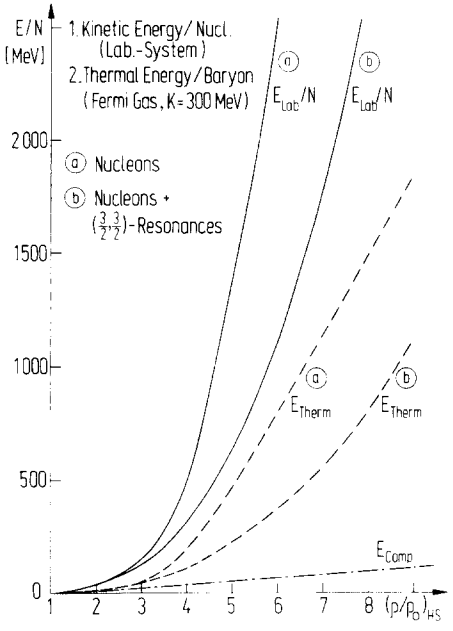

Fig. 13. The projectile energy, the thermal excitation energy (same as in Fig. 6) and the compression energy are drawn as function of the density in the head shock. The connection between the projectile energy and the head shock density is obtained from Eqs. (21–24)

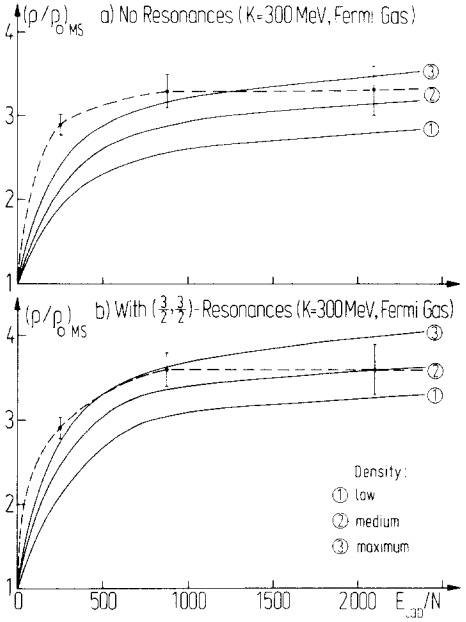

Fig. 14. The density in the main shock front as function of the projectile energy for $K=300$ MeV. In (a) the nuclear matter consists of nucleons only, in (b) also $(\frac{3}{2},\frac{3}{2})$-resonances are included. The full curves are the result of the dynamical calculation with the model described in Ref. 1. The dashed curves are drawn through the "experimental" data (circles). The "experimental" points are obtained via the following prescription: For a given projectile energy the density $(\rho/\rho_0)_{Hs}$ is taken from Fig. 13. The value of $(\rho/\rho_0)_{Hs}$ serves to obtain the head shock velocity $(v_s)_{Hs}$ by using Fig. 7. With the experimental observed angles φ_2 the main shock velocity is calculated according to $(v_s)_{Ms}=\cos\varphi_2\cdot(v_s)_{Hs}$. Finally, the main shock velocity is used to get the main shock density $(\rho/\rho_0)_{Ms}$ from Fig. 7

result.* It could mean, that as soon as there is a density $\rho/\rho_0=3.5$ reached on the sides of the projectile, these compressed matter zones separate from the bulk of the head shock matter and travel sidewards as Mach shock waves.

The densities $(\rho/\rho_0)_{Ms}$ reached in the Mach shock wave are obviously considerable but still smaller than those in the head-shock wave $(\rho/\rho_0)_{Hs}$ (Table 2). The latter are obtained by requesting that the energy of the projectile particles is the same as the energy of the particles in the head shock wave. The energy per

* Even though this "limiting" velocity $(v)_{Ms}\approx 0.58c\approx c/\sqrt{3}$ seems to be identical with the sound velocity of an ultrarelativistic ideal gas, the interpretation of the Mach shock waves as sound-waves has to be ruled out. Since the gas is *not* ultrarelativistic a sound wave would require an extremely high compression constant

$(K=9M_0(v_s)^2_{Ms}\approx 2800$ MeV).

projectile particle

$$E=\frac{M_0 c^2-\tilde{W}_0}{\sqrt{1-(v_{\text{proj}}/c)^2}} \tag{20}$$

is slowed down due to the compression and heat energies, which are given according to (7) for the Fermi gas by

$$E^*=\frac{C}{2\rho_0 \rho}(\rho-\rho_0)^2+\tfrac{1}{2}\beta\,\rho^{-2/3}\,T^2. \tag{21}$$

Therefore, an effective energy per particle within the head shock wave results as

$$E_{\text{eff}}=\frac{M_0 c^2-\tilde{W}_0+E^*}{\sqrt{1-(v_f/c)^2}}. \tag{22}$$

Here, v_f is the velocity of matter in the head shock wave behind the shock front and is measured in the lab-system. It is given by [12]

$$\frac{v_f}{c}=\sqrt{\frac{p(\rho\,W(\rho,T)-\rho_0\,W(\rho_0,0))}{(p+\rho_0\,W(\rho_0,0))\cdot\rho\,W(\rho,T)}}. \tag{23}$$

The flow velocity v_f is shown in Fig. 7 as function of the density. Equating Eq. (20) and (22), we obtain v_f, ρ and v_s of the head shock wave as function of the projectile energy, respectively of v_{proj}. In Table 2 these quantities are listed. Fig. 13 shows the connection between the projectile energy per particle and the head shock density.

Table 2 shows also the flow velocity in the head shock in units of the incoming projectile velocity. Obviously the relative slow-down of the projectile particles while traveling through nuclear matter (head shock) is larger for smaller energies. This seems to be supported by the experimental findings (Table 1, last column).

A strong experimental argument *for shock wave effects* is the emission of particles into backward peaks and their strong 90°-correlation to their forward partners (Figs. 9, 10); they can hardly be explained by other mechanisms. In addition, the assumption of compression waves as nonfrictional collective processes offers a simpler explanation for the observed very low momentum transfer by the projectile nucleus onto the residual target nucleus, than for instance cascade processes producing the same angular distribution.

As an alternative to our shock wave model one might think of target recoil effects. To that end we have calculated the target recoil for the two cases of pure Coulomb interaction and Coulomb interaction with a hard core at $R=R_1+R_2$. The true interaction of such high energetic ions is expected in between these two cases, probably closer to the hard core potential, because of the strong soft core occurring between relativistic nuclei due to the compression effects. In the first case the recoil peaks occur at 90°, in the latter case at 35°, but in both cases the recoil peak is nearly independent of energy, contrary to observation.

Therefore, we conclude, that in the investigated energy range we have observed hydrodynamic effects, i.e. shock waves and Mach cones, and that they are playing an important role amongst the mechanisms of interaction contributing in nucleus-nucleus collisions.

6. Outlook

The presently carried out experiments should be continued and supplemented in various ways. The most general requirement is perhaps to resolve with improving statistics the "fine structure" in the angular distribution of the fragments, so that the predictions on Mach shock waves and their backward satellites can be made even more quantitative. It is well known from hydrodynamics, that second and higher order *Mach shock waves* can occur [19]. They have usually lower densities than the main shock front. This situation is schematically depicted in Figs. 1 and 2. It leads to shock ejection of particles at somewhat larger angles φ_3, φ_4. These higher order Mach shock waves would produce fine structures in the angular distributions. Also it is possible that shock waves in the projectile nuclei can occur. By observing finer structures the now known nuclear compressibility can be determined even more accurately [20]. In principle the compressibility could depend on the nucleon number $A=N+Z$. The observation of Mach cones in different targets and for different projectiles could clarify this question.

Furthermore, the velocity profile of the Mach shock particles which causes dispersion of the shock front, would be interesting to know, as would be the cluster distribution within the various shock waves. Since the densities are rather high, this could tell us something about clustering in nuclear matter as a function of the density. It can be obtained through an analysis of particles and their velocities within the Mach cone. On the other hand, information can also be gathered on the temperature within the shock waves via both the angular widths (Eq. (6)) of the shock cone and the possible proximity-decay of some clusters, which we have already seen. The clustering effects of nuclear matter as a function of its density can be studied by analyzing the angular distributions of the binary and triple tracks. Into the same category belongs the futural observation of emitted pions and nucleonic isobars [2] and their consecutive decay. The possible existence

of density isomeres is of still greater speculative nature, but even more fascinating.

The friendly interest of Prof. Ch. Schmelzer in this work is greatly appreciated.

Note Added in Proof. The position of this peak has been confirmed by recent results from an electronic $\Delta E-E$-type experiment by Gutbrod, Jandoval and Stock (Marburg); and Poskanzer, Sextro and Zebelmann, at the LBL Berkeley: The reaction $^4He + ^{238}U \rightarrow {}^3He$ at $E(^4He) = 0.7$ GeV/N and 1.05 GeV/N shows (broadened) forward peaks in the angular distribution $d\sigma/d\theta$ at $40 \pm 3°$ (1.05 GeV/N) and $38 \pm 5°$ (0.7 GeV/N) for ^{3}He-particles with $60 < E < 100$ MeV/N (private communication by R. Stock).

References

1. Scheid, W., Müller, H., Greiner, W.: Phys. Rev. Lett. **32**, 741 (1974)
   Scheid, W., Hofmann, J., Greiner, W.: Nuclear Shock Waves in Relativistic Heavy Ion Collisions. Proc. of Symp. on Physics with Relativistic Heavy Ions at LBL, Berkeley, Calif., July 1974
2. Hofmann, J., Scheid, W., Greiner, W.: Thermal Excitation of Nucleons in Nuclear Shock Waves, preprint Institut für Theoretische Physik, University Frankfurt/Main, December 1974
3. AgCl-detector cooperation: Schopper, E., Schott, J.U., Wendnagel, Th.: Institut für Kernphysik; Granzer, F.: Institut für Angew. Physik, Universität Frankfurt am Main; Haase, G., Zörgiebel, F.: now Institut für Wissenschaftl. Photographie, TU München
4. Haase, G., Zörgiebel, F., Schopper, E., Granzer, F., Schott, J.U., Wendnagel, Th.: Photogr. Sci. Eng. **17**, 409 (1973)
5. Schott, J.U.: IKF-Report 33. Thesis Frankfurt/Main 1974
6. Schopper, E., Schott, J.U.: To be published in Nucl. Inst. and Methods
7. Barkas, W.H.: Nuclear Research Emulsions, Vol. I, p. 387ff. New York and London: Acad. Press 1963
8. Chapline, G.F., Johnson, M.H., Teller, E., Weiss, M.S.: Phys. Rev. D**8**, 4302 (1973)
9. This is analogous to the von Grotthus-mechanism of electric conductivity in strong electrolytes: v. Grotthus, Th.: Ann. Chim. **58**, 54 (1806)
10. This contradicts to some extent the supposition of Siemens, P., Bondorf, J., Bethe, H.A.: Discussion at the Bear Mountain Meeting on Physics with Relativistic Nuclei, November 1974, organized by Brookhaven Nat. Lab. and by Columbia University
11. Stöcker, H.: Diploma thesis, Inst. f. Theoretische Physik, Univ. Frankfurt/M., 1975
12. Landau, L.D., Lifschitz, E.M.: Hydrodynamics and Statistical Physics. London: Pergamon 1958
13. Rankine, W.J.M.: Phil. Trans. Roy. Soc. (London) **160**, 277 (1870)
14. Hugoniot, J.: J. Ecole Polytech., Cahier **57**, 1 (1887)
15. Otterlund, I., Resman, R.: Arkiv för Physik **39**, 265 (1969)
16. Kullberg, R., Otterlund, I.: Z. Physik **259**, 245 (1973)
17. Heckman, H.H.: Proc. 5th Int. Conference on High Energy Physics, Uppsala (Sweden) 1973
18. Le Couteur, K.J.: Proc. Phys. Soc. London A**65**, 718 (1952)
19. Hayes, W.D., Probstein, R.F.: Hypersonic Flow Theory. New York-London: Academic Press 1959
20. The knowledge of the nuclear compressibility is of considerable importance also in astrophysics for star models. See e.g. Heintzmann, H., Hillebrand, W., El Eid, M.F., Hilf, E.: Z. f. Naturforschung **29**a, 933 (1974)
21. Baumgardt, H.G.: Diploma-thesis, Frankfurt, in preparation

H.G. Baumgardt
J.U. Schott
Y. Sakamoto
E. Schopper
Institut für Kernphysik der Johann Wolfgang Goethe-Universität
D-6000 Frankfurt/Main 90
August Euler-Straße 6
Federal Republic of Germany

H. Stöcker
J. Hofmann
W. Scheid
W. Greiner
Institut für Theoretische Physik
der Johann Wolfgang Goethe-Universität
D-6000 Frankfurt/Main 1
Robert-Mayer-Straße 8-10
Federal Republic of Germany